Unsteady surface pressure measurements of propeller-wing interaction with a MEMS-embedded sleeve

Aerospace Science and Technology 175 (2026) 111980

Contents lists available at ScienceDirect

Aerospace Science and Technology

journal homepage: www.elsevier.com/locate/aescte

Original article

Unsteady surface pressure measurements of propeller-wing interaction with a MEMS-embedded sleeve

P. Comunian [a,*], G. Cafiero [a], J. Serpieri [a], F. Avallone [a], R. Zamponi [b,c], D. Ragni [b], T. Sinnige [b]

[a] Department of Mechanical and Aerospace Engineering, Politecnico di Torino, Corso Duca degli Abruzzi 24, Turin, 10129, Italy
[b] Delft University of Technology, Kluyverweg 1, Delft, 2629 HS, The Netherlands
[c] von Karman Institute for Fluid Dynamics, Waterloosesteenweg 72, Sint-Genesius-Rode, B-1640, Belgium

ARTICLE INFO

Communicated by: Dr. Tianxiang Hu

PACS:
0000
1111

2000 MSC:
0000
1111

Keywords:
MEMS
Unsteady pressure measurement
Propeller-wing interaction

ABSTRACT

This work investigates the unsteady aerodynamic interaction that arises from the impingement of a propeller slipstream on a wing. To this end, an innovative measuring device for unsteady pressure is deployed, comprising a flexible printed circuit board sleeve embedded with MEMS pressure sensors and microphones. The device performance is validated against conventional measurement techniques. The wing is a benchmarked NACA 63_3018 airfoil-based model, and the propeller is the TUD-XPROP-S. In addition to pressure measurements, oil flow visualizations are performed to elucidate the flow pattern on the wing when the propeller operates at advance ratios of 0.8 and 1.8, and nominal blade pitch angles of 30° and 45°. The measurements reveal the formation of a laminar separation bubble on the portion of the wing not washed by the propeller slipstream. The flow is seen to remain attached on the advancing blade side, at least for the tested angles of attack. The microphone measurements capture the trace of the propeller's tip vortices over the wing and the deformation of the slipstream over the wing. This work serves a dual purpose. Firstly, presenting an innovative measuring device for unsteady pressure, as the sensor-embedded sleeve requires minimal installation efforts and allows for a comprehensive measurement of the unsteady surface pressure field. Secondly, discussing the complex spatio temporal interaction that is formed from the impingement of a propeller slipstream onto a wing.

1. Introduction

Propeller-driven aircraft are expected to play a key role in the electrification of the aviation industry [1,2]. A proper understanding of the interaction effects between a propeller and a downstream wing is crucial to correctly assess the performance of an aircraft [3].

The interaction between a tractor propeller and a downstream wing is mutual [4]. From a time-average perspective, the propeller induces axial momentum and swirl to the flow, increasing the dynamic pressure and changing the effective angle of attack locally seen by the wing. This changes the loading distribution over the wing in an anti-symmetrical way [5]: the up-going blade induces upwash downstream, while the down-going blade induces downwash. For the remainder of this paper, these regions are labelled up-going blade side (UBS) and down-going blade side (DBS), respectively. The combination of these effects leads to an uneven loading distribution along the span, which can lead to an increase in lift [6–10]. On the other hand, the wing induces upwash upstream, yielding an increase in the angle of attack seen by the propeller, which changes the load distribution on the propeller disk in an asymmetric way [11]. The down-going blade sees an increased angle of attack and dynamic pressure, generating an increased aerodynamic loading, while, for the up-going blade, the opposite is true. In addition, the wing-induced pressure field locally reduces the effective inflow velocity at the propeller plane, causing additional non-uniformity in the blade loading distributions.

Several studies (e.g.[12–14]) have shown that the time-average approach is not sufficient to fully describe the physics of the propeller slipstream interaction with the lifting element, as it fails to account for the unsteady pressure distribution. This can have an impact on the vibrations transmitted to the structure, on the noise emissions [15] due to the fluctuating pressure field, and induce fluctuations of the aerodynamic forces [16]. In this regard, experimental data is valuable, as numerical simulations involving propellers are often computationally expensive due to the unsteadiness and the three-dimensionality of the flow. To correctly assess the described flow physics, high temporal and spatial resolution are needed.

* Corresponding author.
E-mail address: paolo.comunian@polito.it (P. Comunian).

https://doi.org/10.1016/j.ast.2026.111980
Received 6 October 2025; Received in revised form 13 January 2026; Accepted 20 February 2026
Available online 28 February 2026

Knowing the pressure distribution over a wing allows to evaluate many of the effects so far discussed. In addition, measuring the unsteady surface pressure acting on a surface can also provide insight to topics unrelated to propeller-wing interaction, as are the radiated noise [17,18], to vibrations transmitted to the supporting structure [19,20], or to the local behaviour of the flow [21]. Surface pressure is usually measured through pressure taps that populate the surface of the test object. Besides altering the surface and inner characteristics of the model, this approach prioritizes accuracy at low frequencies (< 500 Hz), owing to the length of the connecting tubes, which usually affects the frequency response of the system [22]. Microphones can instead be used to measure unsteady pressure fluctuations at frequencies as large as 20 to 25 kHz. However, a typical electret microphone only measures pressure fluctuation relative to the time-averaged value with a limited amplitude range. A common installation for microphone capsules is a pinhole cap. The microphone is installed inside a cavity and only a small hole connects it to the external surface [23,24]. This approach requires space beneath the surface and introduces a maximum cut-off frequency due to acoustic resonance in the cavity [25,26]. Sensors that enable pressure measurement for a wider range of amplitudes and with a high-frequency response exist, yet, they are expensive and it might not be possible to fit them in all models due to geometric constraints. Other approaches, such as pressure-sensitive paints (PSP), offer the possibility of having spatio-temporal resolved data up to a few kHz. However, some aspects of the technology and its implementation still pose technical challenges, namely the binder used to make the PSP [27], the thermal sensitivity, and the need to perform an *in situ* calibration, making it a more complex approach with respect to the methodologies previously discussed.

An alternative to the approaches so far described can be found in microelectromechanical systems (MEMS). The advancements in MEMS technology [28] represent an opportunity to use miniaturized components that can be installed within an integrated circuit board. They are used in a wide range of applications, including automotive, wearable devices, smartphones, and different kinds of sensors such as pressure sensors and microphones [29]. The applicability of MEMS microphones for aeroacoustic measurements has already been demonstrated [30]. Unsteady surface pressure measurements have also been achieved with MEMS components, as shown in [31], while in-flight tests using MEMS pressure sensors have also been performed [32]. Nevertheless, all the discussed applications required an *ad hoc* model or system.

This work presents a sensor-embedded sleeve (SES) developed at Delft University of Technology, made from a flexible printed circuit board (PCB) containing MEMS pressure sensors and microphones. The novelty of this sensor lies in the ease of installation without requiring any modifications to the target surface. In addition, the system is fully reusable, making it a highly versatile measuring device. The combination of MEMS microphones and pressure sensors results in comprehensive and cost-effective measurements of both steady and unsteady surface pressure.

The technology is validated by installing the SES on a benchmarked NACA 63_3018 airfoil-based model. The model, described in [33], is instrumented with pressure taps, allowing for a direct comparison of the pressure distribution. The measured wall pressure spectra were also validated using empirical laws based on the integral parameters of the boundary layer [34,35].

Finally, the SES is used to study the interaction between a propeller slipstream and a downstream wing. A specific point that requires further investigation is the temporal analysis of the unsteady pressure in the slipstream impingement region. As discussed, the propeller slipstream is highly non-uniform in space and time and represents a source of tonal (coherent) and broadband (turbulent) fluctuations seen on the wing surface [12]. By using the SES, good spatio-temporal resolution is achieved, which contributes to the understanding of propeller-wing interaction.

2. Methodology and test cases

2.1. PCB flexible sensor embedded sleeve

The SES comprises 18 Knowles SPW0690LM4H-1 digital microphones and 6 Bosch BMP390 barometric pressure sensors. The layout of the sensor sleeve is shown in Fig. 1a. It consists of a rectangular PCB sleeve of 170 mm in width by 350 mm in length. The MEMS sensors are installed on rigid, non-flexible surfaces, while the rest of the sleeve is flexible. The 18 microphones are arranged in three rows of six microphones each, with a non-uniform spacing, as indicated in Fig. 1a. The sensor was designed to be easily installed on any target surface. In the present case, it is deployed on a wind tunnel model of a wing; for this reason, a larger central flexible gap was included to account for the curvature around the leading edge. The entire sleeve is divided into four ribbons, facilitating the installation of the sensor.

The absolute pressure sensors have dimensions of 2.5 mm x 3 mm by 0.85 mm in height, while the microphones are 2 mm x 2 mm by 0.75 mm. The chosen microphone has its sensing element on the same side that is in contact with the PCB, which allows it to be installed flush-mounted. It is connected to the exterior through a hole drilled in the PCB as depicted

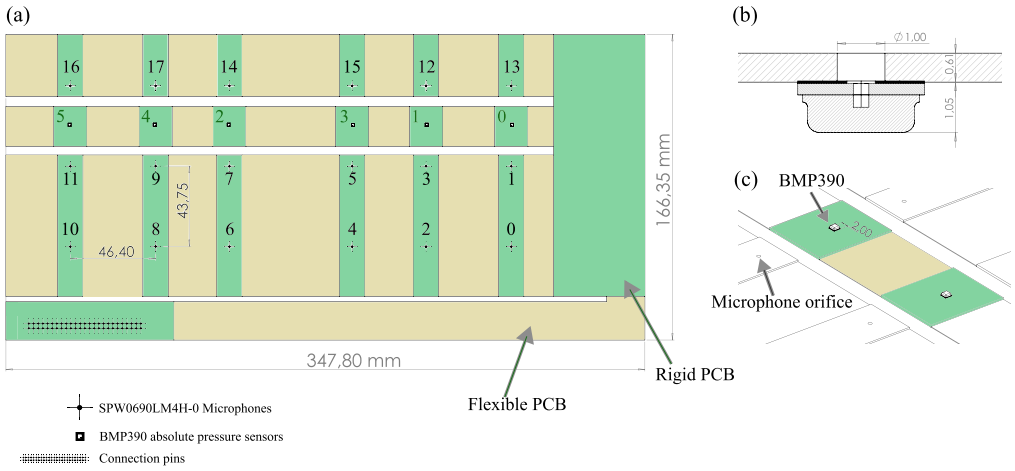

Fig. 1. (a) Sensor embedded sleeve and details of (b) microphones' installation and (c) BMP390 pressure sensors and microphones. The indicated distances and sizes are measured in mm. The black numbers indicate the microphone channel, while the green numbers indicate the absolute pressure sensor's channel. (For interpretation of the references to colour in this figure legend, the reader is referred to the web version of this article.)

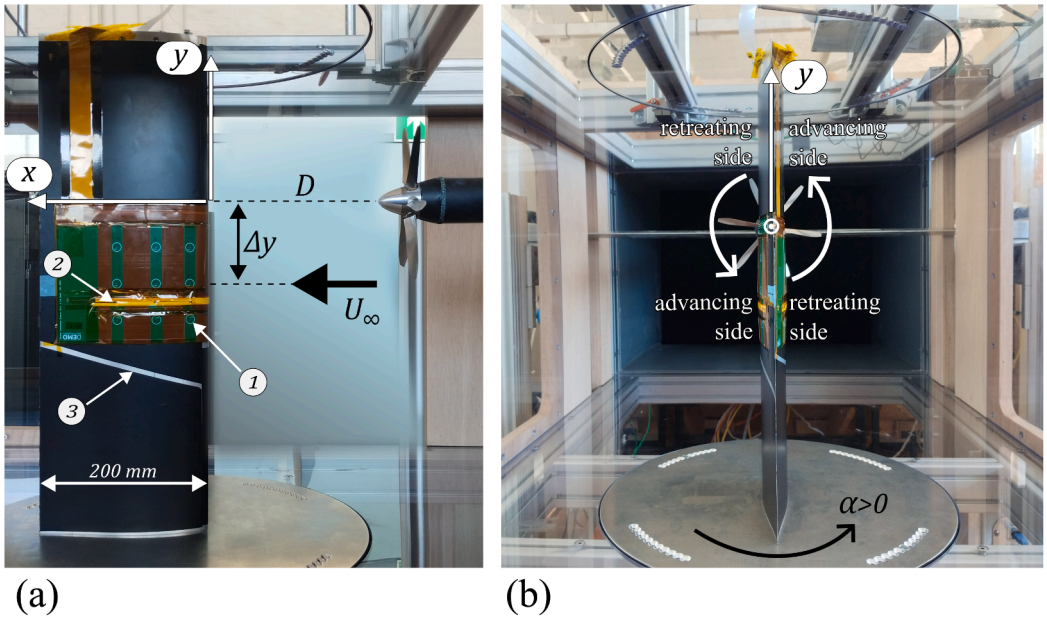

Fig. 2. Experimental setup with the propeller at the highest position along the span: (a) Side view of the pressure side and (b) downstream view indicating the propeller rotation direction and the convention adopted for positive angles of attack. (1) microphone, (2) absolute pressure sensor, (3) pressure taps.

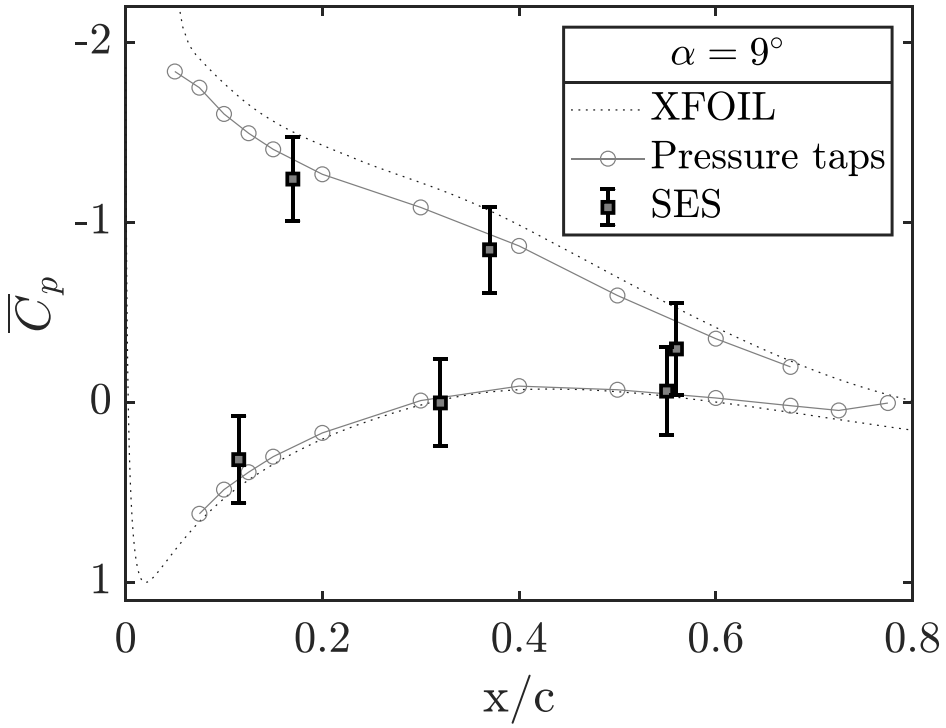

Fig. 3. Comparison between the pressure coefficient measured with pressure taps (circles) and with the SES (squares): nacelle-only case as well as estimated with XFOIL (dotted line).

in Fig. 1b. The pressure sensor is installed on the opposite side of the PCB relative to the microphone due to the location of the sensing element being opposite to the side that is soldered to the PCB. A detail of the installation is shown if Fig. 1c. This installation arrangement results in a thickness of 2.5 mm for the SES from the bottom of the microphone to the top of the pressure sensor.

The absolute pressure sensors have a full scale ranging from 300 to 1250 hPa, and an absolute error of ±50 Pa. The microphone's calibration frequency response is flat between 100 Hz and 10 kHz, with an amplification of -3 dB and 3 dB at 45 Hz and 15 kHz, respectively. The peak resonant frequency is expected at 26 kHz. Finally, the total harmonic distortion (THD) is below 2% for a measured SPL of 125 dB for frequencies ranging from 100 Hz to 4 kHz. At higher frequencies, the THD increases, never exceeding 4% within the measurable range.

2.2. Facility and model

The SES was installed on a wing model based on a NACA 63_3018 airfoil with a chord of 200 mm and equipped with pressure taps arranged to measure the chord-wise pressure distribution (further details can be

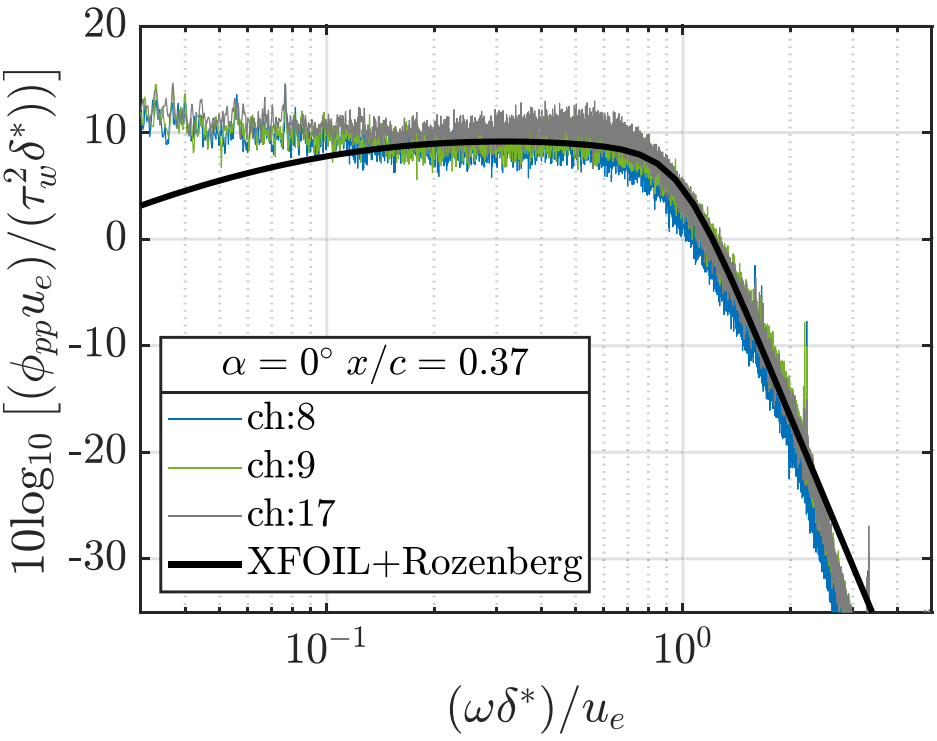

Fig. 4. Comparison between the wall pressure power spectral density $\phi_{pp}(\omega)$ measured and estimated at $\alpha = 0°$ at x/c = 0.37: nacelle-only case.

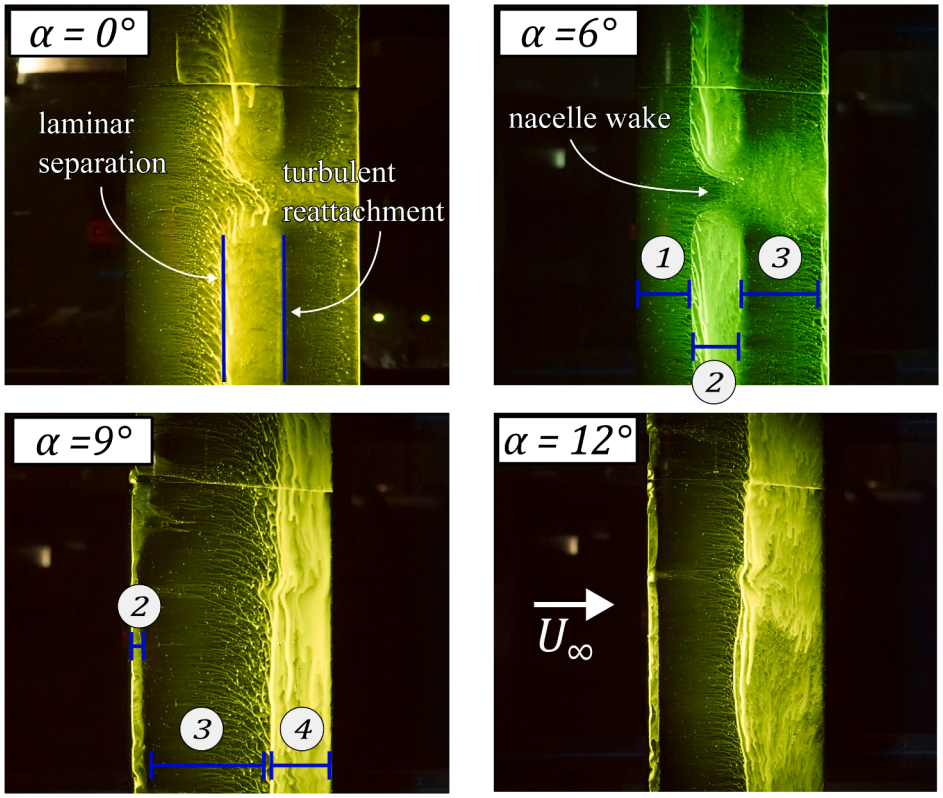

Fig. 5. Oil-flow visualization on the suction side, nacelle-only cases: (1) laminar flow, (2) laminar separation bubble, (3) turbulent flow, and (4) trailing edge separated flow.

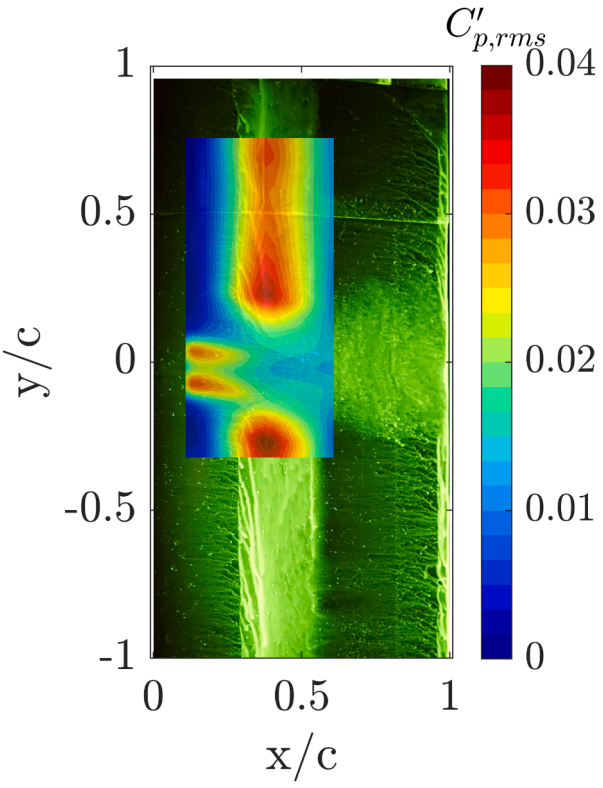

Fig. 6. Overlay of the unsteady pressure coefficient rms $C'_{p,rms}$ on the oil flow visualization at $\alpha = 6°$, nacelle-only.

found in [33]). The wing was placed inside the SLT wind tunnel at TU Delft and mounted in a wall-to-wall arrangement to minimize the effects of the boundaries. The test section of the SLT has a rectangular geometry, with 90 cm in width and 60 cm in height; the total length is 180 cm. The wing model is mounted on two circular side plates, embedded into the tunnel's walls with a 50 cm diameter that act as turntables, allowing for changes in the angle of attack in steps of 3 degrees.

A TUD-XPROP-S propeller [36,37] was used for the experiments. It is a 6-bladed propeller, with a 203.2 mm (8-inch) diameter (D). The propeller was placed at a distance equal to one diameter upstream of the wing's leading edge (LE), such that the accelerated flow by the propeller is directed towards the wing. In the chosen reference frame, indicated in Fig. 2a, the $x-$axis and the $y-$axis are aligned with the propeller rotation axis and the wing spanwise direction, respectively, with the origin placed at the LE. It is worth noting that the propeller is mounted such that it always stays at a zero degree angle of attack relative to the freestream and does not change orientation together with the wing.

The propeller drive train is equipped with an encoder allowing for direct control of the rotational velocity (n). A one-per-revolution trigger signal from the encoder was acquired in sync with other measurements to conduct a phase-averaging of the sampled data.

The propeller rotation direction and the positive angle of attack convention are indicated in Fig. 2b. The up-going blade side corresponds to the suction side for $y > 0$, while the down-going blade side to $y < 0$. Fig. 2b also shows the convention adopted for advancing and retreating sides relative to the propeller's rotation direction. The terminology, advancing and retreating side, refers to the direction the blade is moving with respect to the wing. If the blade is moving away from the wing's surface, that side is labelled as the retreating side, while if it is moving towards it, then that side is indicated as the advancing side. Conversely, UBS and DBS indicate if the propeller blade is moving from the pressure side to the suction side or from the suction side to the pressure side, respectively.

Table 1
Pressure and microphones chord-wise locations.

	(x/c)		
Suction side	0.17	0.37	0.56
Pressure side	0.12	0.32	0.55

2.3. Pressure measurements

The pressure taps in the wing model (described in [33]) were used for comparison with the pressure data obtained with the SES. The pressure taps were connected to two 16-channel differential pressure transducers with 2.5 kPa range and 0.25% full-scale accuracy (±6 Pa); the total sampling time was 60 s. Before every measurement conducted with the SES, a wind-off offset measurement was taken. To reduce data volume, the measurements with the SES were taken for 30 s instead of 60 s. It was confirmed that this was sufficient to obtain converged statistics.

To measure the pressure field over a significant spanwise extent of the wing, it was chosen to move the propeller along the spanwise direction (Δy in Fig. 2a) to simulate the movement of the sensor of the wing. This was considered acceptable given the quasi-2D installation of the wing. This approach leads to a spanwise resolution of 12 mm (6% of the chord) for the pressure captured from the SES.

The microphones were calibrated by evaluating the frequency response amplitude to a sinusoidal pressure input from a GRAS pistonphone at 1 kHz and 114 dB. The chord-wise location of the measuring points is indicated in Table 1.

The results obtained from the pressure taps and from the absolute pressure sensors and microphones on the SES will be reported in terms of the pressure coefficient (C_p) according to:

$$C_p(\mathbf{x}, t) = \frac{p(\mathbf{x}, t) - p_\infty}{q_\infty}, \tag{1}$$

where q_∞ and p_∞ are the dynamic pressure and the static pressure of the flow, respectively.

Wall pressure spectrum

The pressure spectrum measured beneath the boundary layer developed over the wing was compared against the empirical relations obtained from the adverse pressure gradient model (APG) proposed by Rozenberg et al. [34]. As discussed in [35], the model is based on a relation between the power spectral density associated with the pressure signal (ϕ_{pp}), the integral parameters of the turbulent boundary layer, and the fluid properties. Namely,

$$\phi_{pp}(\omega) = F\left(\delta, \delta^*, \theta, \rho, \nu, \tau_w, \partial_x p, \Pi\right). \tag{2}$$

Here, ω is the angular frequency, δ is the boundary layer thickness, δ^* is the displacement thickness, θ is the momentum thickness, ρ and ν are the fluid density and kinematic viscosity, respectively, τ_w is the skin friction, $\partial_x p$ is the pressure gradient along the wall parallel direction, and Π is the wake strength parameter.

Due to the absence of flow field measurements, the missing parameters were estimated using XFOIL [38] with a forced transition setting. The boundary layer thickness was computed according to [39], while the wake strength parameter was estimated using the same relation used to derive the model for $\phi_{pp}(\omega)$ proposed by Rozenberg et al. [34].

Triple decomposition

For the cases in which the propeller is running (from now on referred to as propeller-on), the unsteady pressure fluctuations $p'(\mathbf{x}, t)$ can be subdivided into two components: a coherent fluctuation, associated with the propeller rotation, and a stochastic fluctuation. These two can

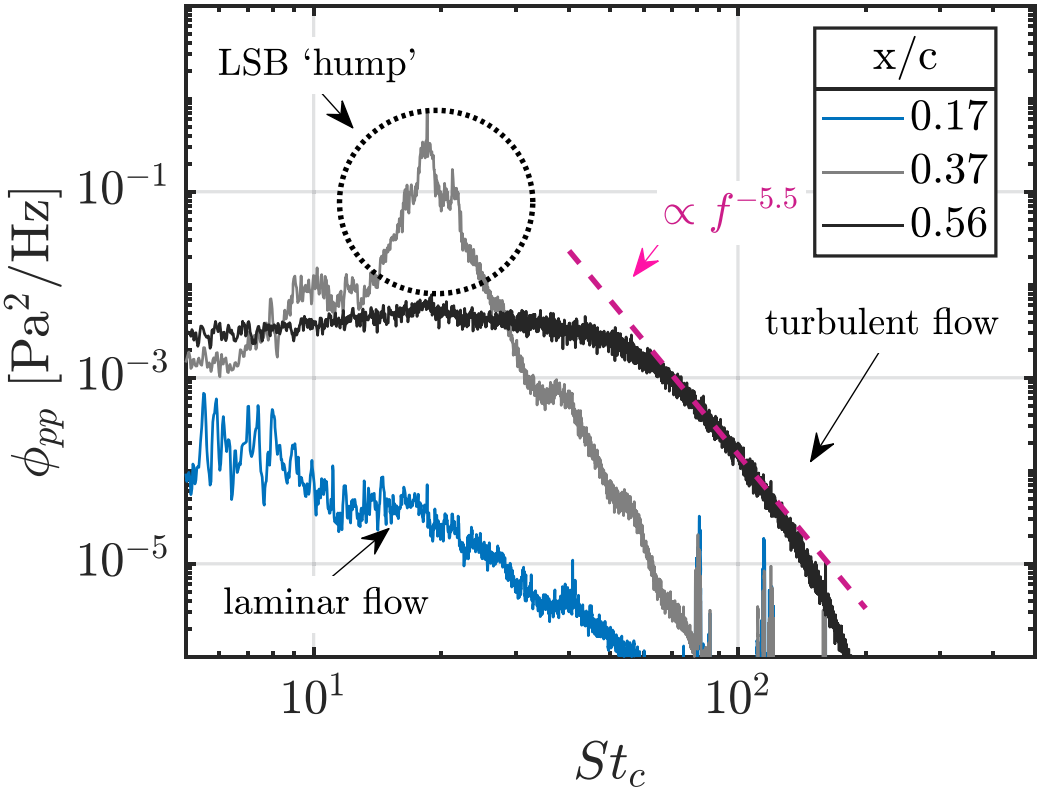

Fig. 7. Wall pressure PSD measured at $y/c = 0.4$ for $\alpha = 6°$ at 20 m/s, nacelle-only case.

be separated by applying a triple decomposition [40–42]. For the pressure in time and space, the decomposition reads:

$$p(\mathbf{x},t) = \overline{p}(\mathbf{x}) + p'(\mathbf{x},t) \tag{3}$$

$$= \overline{p}(\mathbf{x}) + \tilde{p}(\mathbf{x},t) + p''(\mathbf{x},t). \tag{4}$$

The right-hand side terms in Eq. (4) correspond to the time-average $\overline{p}(\mathbf{x})$, phase-correlated $\tilde{p}(\mathbf{x},t)$, and stochastic $p''(\mathbf{x},t)$ components, respectively:

$$\overline{p}(\mathbf{x}) = \lim_{T\to\infty} \frac{1}{T} \int_0^T p(\mathbf{x},t)\, dt \tag{5}$$

$$\tilde{p}(\mathbf{x},t) = \langle p(\mathbf{x},t)\rangle - \overline{p}(\mathbf{x}) \tag{6}$$

$$\langle p(\mathbf{x},t)\rangle = \lim_{N\to\infty} \frac{1}{N} \sum_{k=0}^{k=N} p(\mathbf{x}, t + k\tau) \tag{7}$$

$$p''(\mathbf{x},t) = p(\mathbf{x},t) - \langle p(\mathbf{x},t)\rangle \tag{8}$$

In Eq. (7), the operator $\langle\cdot\rangle$ indicates phase averaging according to a characteristic time τ. It is worth noting that for signals for which the time average is zero, the phase-average and the phase-correlated signals coincide. It can be shown that the sum of the root mean square (rms) of the decomposed fluctuations, namely p''_{rms} and $\tilde{p}_{rms}$, is equivalent to p'_{rms}. This is also expected, as p'' and $\tilde{p}$ are uncorrelated by definition.

2.4. Oil flow visualization

Oil flow visualization is used to elucidate the flow pattern on the wing. This is useful to identify the flow direction, laminar to turbulent transition lines, and flow separation regions. The oil mixture used is a combination of paraffin and a few drops of A-680 fluorescent additive, with the exact quantity being chosen on a case-by-case basis. A UV spotlight was used to provide the necessary illumination, while the images were captured with a 20 MP reflex camera. Lastly, the sensor sleeve was removed for the oil flow visualization images. Propeller-on and nacelle-only cases were evaluated. With this, a comparison with the data obtained by the SES is possible.

Table 2
Propeller operating conditions.

Configuration	$Re_{\frac{r}{R}=0.7}$	$M_{\frac{r}{R}=0.7}$	T_c	n [Hz]
$\beta_{\frac{r}{R}=0.7} = 30°$ & $J = 0.8$	$60 \cdot 10^3$	0.17	0.99	123
$\beta_{\frac{r}{R}=0.7} = 45°$ & $J = 1.8$	$32 \cdot 10^3$	0.09	0.14	54.7

2.5. Test cases

The tests were carried out at a free stream velocity (U_∞) of 20 m/s, corresponding to a Reynolds number based on the wing's chord equal to $2.68 \cdot 10^5$. Transition phenomena must be taken into account, as, purposely, no transition trip was installed.

In total, 19 propeller positions with a step of 12 mm were tested. For each position, 18 microphone measurements and 6 pressure sensor measurements were captured. This approach leads to a spanwise resolution for the microphones ranging from 3 mm to 12 mm, deemed acceptable for our purpose, albeit not improving the chordwise resolution.

Two propeller-on cases were studied. Firstly, a case with a blade pitch angle at 70% ($\beta_{\frac{r}{R}=0.7}$) of 30° and an advance ratio ($J = U_\infty/(nD)$) of 0.8. Secondly, a case with $\beta_{\frac{r}{R}=0.7} = 45°$ operated at $J = 1.8$. These cases were chosen since they represent conditions that are close to the propeller's maximum efficiency, which should result in a more coherent slipstream [13]. Far from the optimal operating conditions, the blades are likely to stall in some regions, which would lead to a less coherent and more turbulent slipstream. The differences between the cases are summarized in Table 2, indicating the Reynolds (Re) and Mach (M) numbers at 70% of the blade radius, the thrust coefficient ($T_c = T/(q_\infty \pi R^2)$) and the revolutions per second n.

The parameters in Table 2 were obtained from reference data and exploiting the BEMT code described in [6]. Due to the higher thrust coefficient, the first case ($J = 0.8$) will induce a higher velocity to the flow, and the tip vortices impinging on the wing will be more frequent as

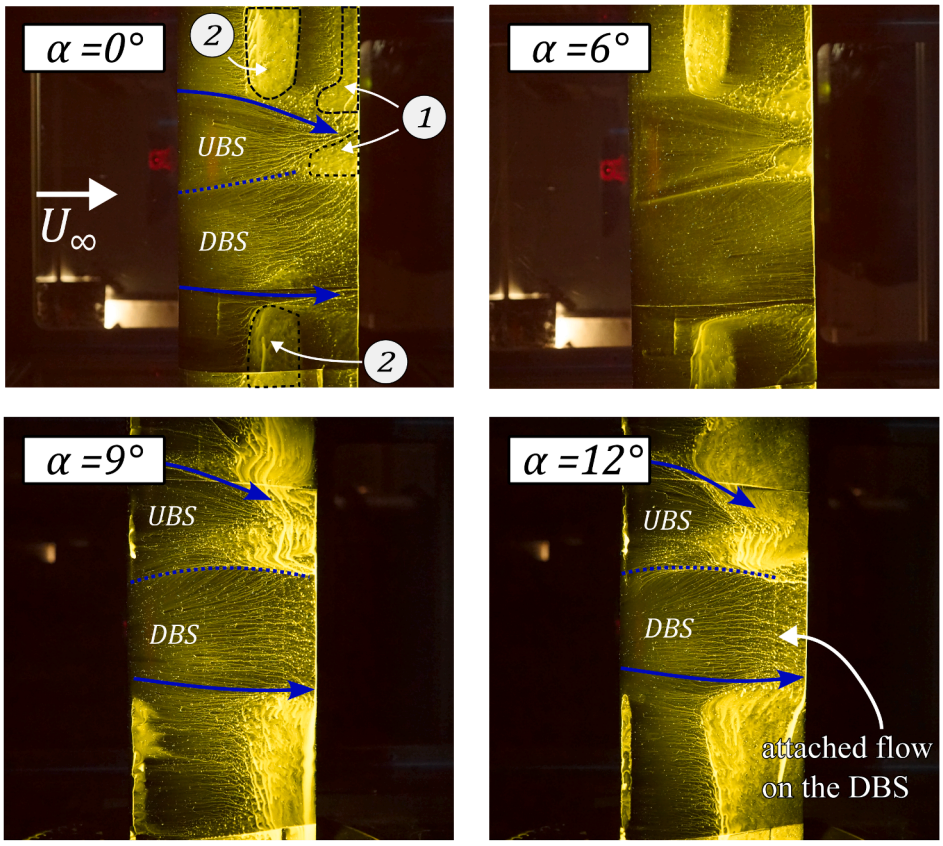

Fig. 8. Oil-flow visualization on the suction side, propeller-on cases with $\beta_{\frac{r}{R}=0.7} = 30°$ at $J = 0.8$. (1) separated flow at the trailing edge. (2) separation bubble. Blue arrows indicate the approximate slipstream edges over the wing.

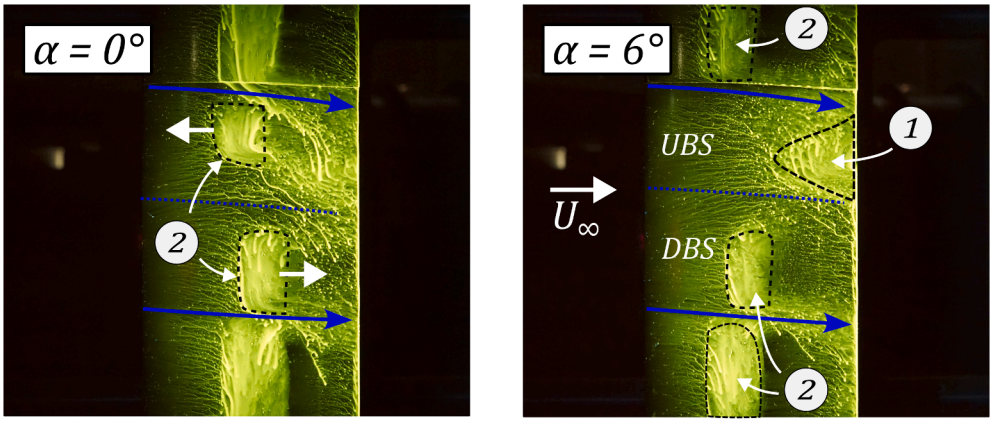

Fig. 9. Oil-flow visualization on the suction side, propeller-on cases with $\beta_{\frac{r}{R}=0.7} = 45°$ at $J = 1.8$. (1) separated flow at the trailing edge. (2) separation bubble. Blue arrows indicate the approximate slipstream edges over the wing.

the advance ratio is lower. Lastly, due to the different blade pitch angle and advance ratio, the slipstream helix angle [13] will be less steep for the case at $J = 1.8$.

In addition to the propeller-on cases, nacelle-only cases for angles of attack of 0°, 6°, 9°, and 12° were also evaluated. For these cases, the propeller was removed while maintaining a dummy spinner, which is geometrically equivalent to removing the blades. The same measurement procedure was followed with respect to that used for the propeller-on cases. A summary of the test condions is given in Table 3.

Table 3
Test conditions. The superscripts *a* and *b* indicate configurations used exclusively together.

Parameter	nacelle-only	propeller-on
Reynolds number Re_c [-]	$2.68 \cdot 10^5$	$2.68 \cdot 10^5$
Free-stream velocity U_∞ [m/s]	20	20
Angle of attack α [deg]	0, 6, 9, 12	0, 6, 9, 12
Advance ratio J [-]	–	0.8^a, 1.8^b
Blade pitch at $r/R = 0.7$ [deg]	–	30^a, 45^b

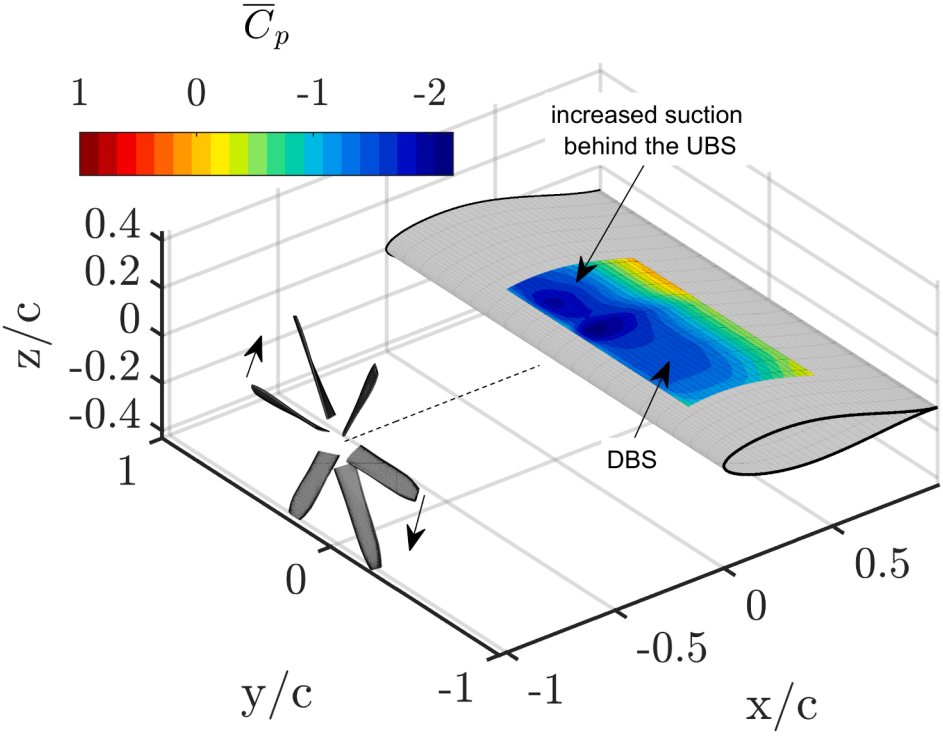

Fig. 10. Time-averaged pressure coefficient ($\overline{C}_p$) distribution obtained from the pressure sensors. Wing at $\alpha = 6°$ and propeller with $\beta_{\frac{r}{R}=0.7} = 30°$ operating at $J = 0.8$.

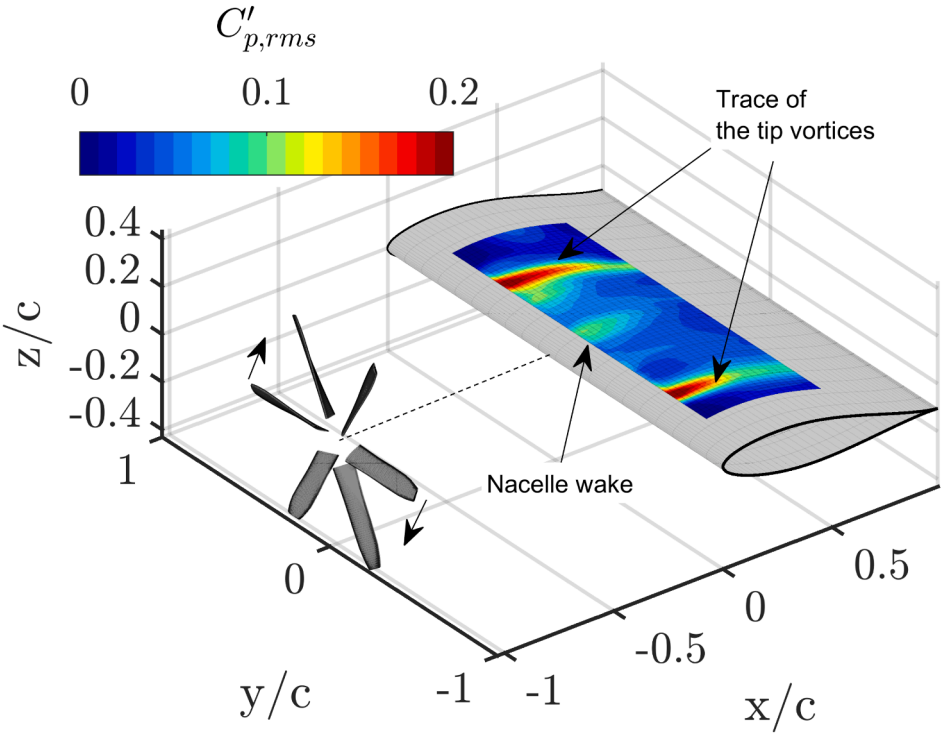

Fig. 11. Rms of the unsteady pressure coefficient ($C'_{p,rms}$) evaluated from the microphones. Wing at $\alpha = 6°$ and propeller with $\beta_{\frac{r}{R}=0.7} = 30°$ operating at $J = 0.8$.

3. Validation tests

To validate the outputs from the absolute pressure transducers on the SES, the results were compared to those obtained from the pressure taps and XFOIL computations. The chordwise distribution of time-averaged pressure coefficient ($\overline{C}_p$), measured at an angle of attack of $\alpha = 9°$, is shown in Fig. 3. The values measured with the pressure taps are directly compared with the ones obtained by the SES, showing that the SES is sensitive enough to capture the static pressure distribution. The average absolute difference between the $\overline{C}_p$ measured by the SES and by the pressure taps is 0.084. The uncertainty bar on each data point represents the sum of the standard deviation and the absolute error in the

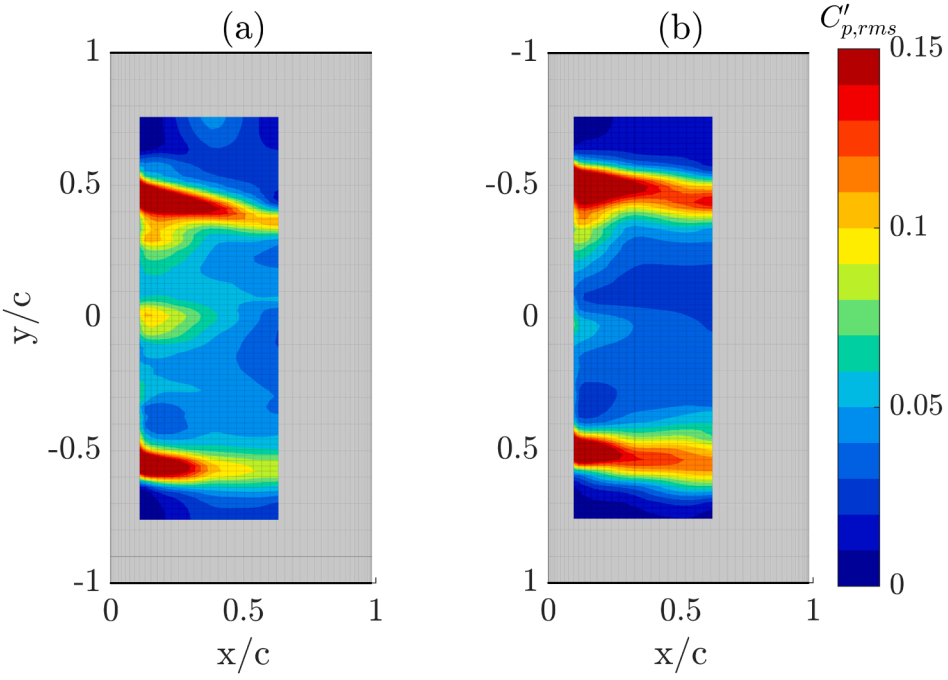

Fig. 12. Rms of the unsteady pressure coefficient ($C'_{p,rms}$). Wing at $\alpha = 6°$ and propeller with $\beta_{\frac{r}{R}=0.7} = 30°$ operating at $J = 0.8$: (a) Suction side and (b) pressure side.

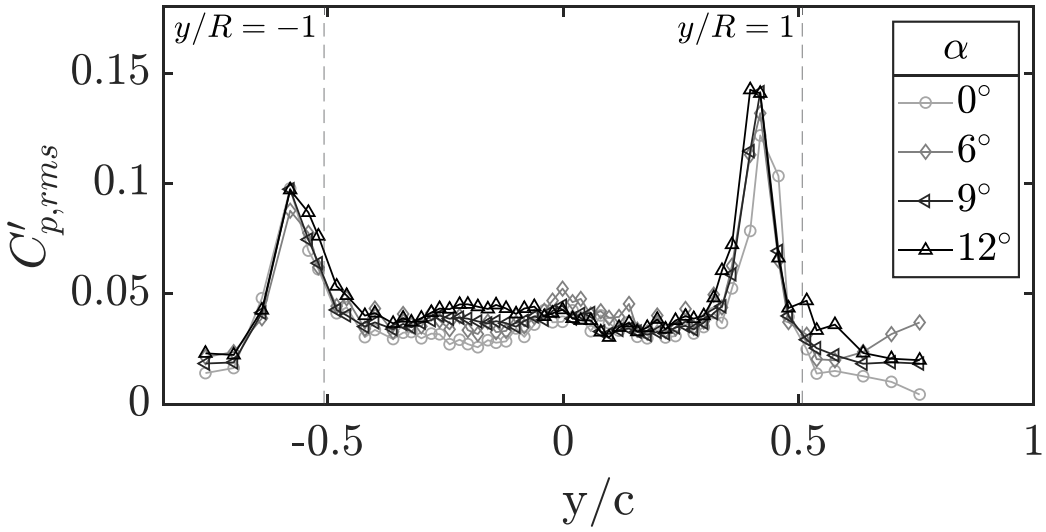

Fig. 13. Rms of the fluctuating pressure coefficient ($C'_{p,rms}$) measured on the suction side at $x/c = 0.37$ for the case with $\beta_{\frac{r}{R}=0.7} = 30°$ at $J = 0.8$.

measured value. The latter is ±50 Pa for the BMP390 pressure sensor; in this regard, it would be better suited to applications where the pressure differentials involved were greater, as this error would represent a smaller fraction of the measured value.

A basis of comparison for the measurements obtained with the microphones was obtained by leveraging the model proposed by Rozenberg [34] to estimate the power spectral density (PSD) of the pressure fluctuations inside a boundary layer with an adverse pressure gradient.

The PSD of the measured wall pressure fluctuations at an angle of attack $\alpha = 0°$ at a chordwise position $x/c = 0.37$ is shown in Fig. 4. It is obtained by the Welch algorithm, using 64 segments and a Hanning window with 50 % overlap, leading to a final spectral resolution of 2.82 Hz.

The evaluated PSD is normalized by the boundary layer parameters obtained from XFOIL and compared with the prediction provided by Rozenberg's model. Although the $\overline{C}_p$ obtained from XFOIL shows an offset with respect to the one obtained experimentally, as seen in Fig. 3 on the suction side, the pressure gradient is well reproduced, which is what is ultimately used for Rozenberg's model.

The experimental data correspond to the signals sampled by three different microphones at different relative positions between the nacelle and the sensor's center line, such that the microphones are all at $y = 0$ and $x/c = 0.37$. The predicted and measured PSD are in good agreement for normalized frequencies $(\omega\delta^*)/u_e$ higher than 10^{-1}, as in this range only the turbulent fluid-related fluctuations are expected. For frequencies lower than this, it is likely that other spurious sources of noise, such as the wind tunnel driving motor or general vibrations of the tunnel, are also captured by the microphones. This comparison shows how the microphones capture the wall pressure spectrum in both amplitude and frequency.

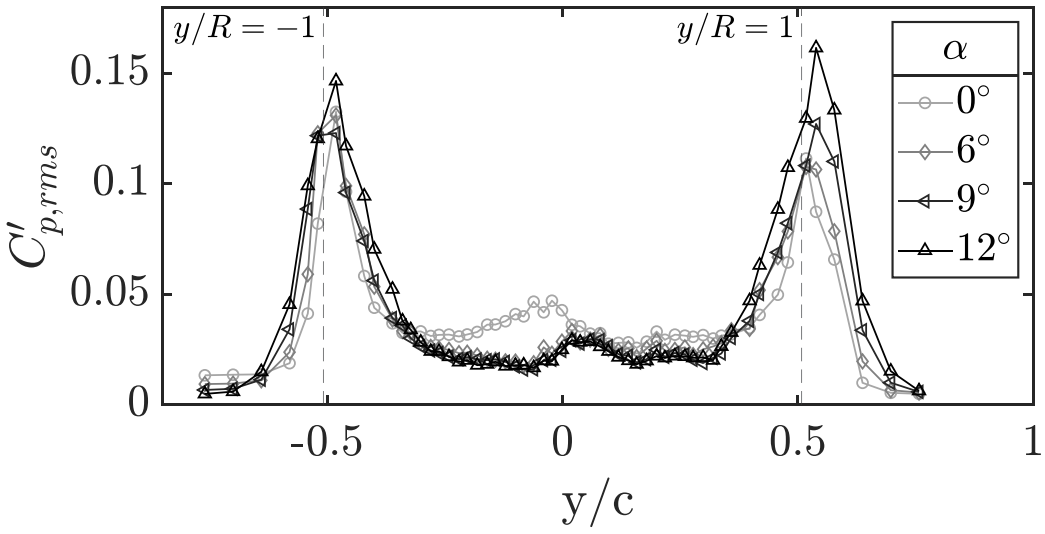

Fig. 14. Rms of the fluctuating pressure coefficient ($C'_{p,rms}$) measured on the pressure side at $x/c = 0.32$ for the case with $\beta_{\frac{r}{R}=0.7} = 30°$ at $J = 0.8$.

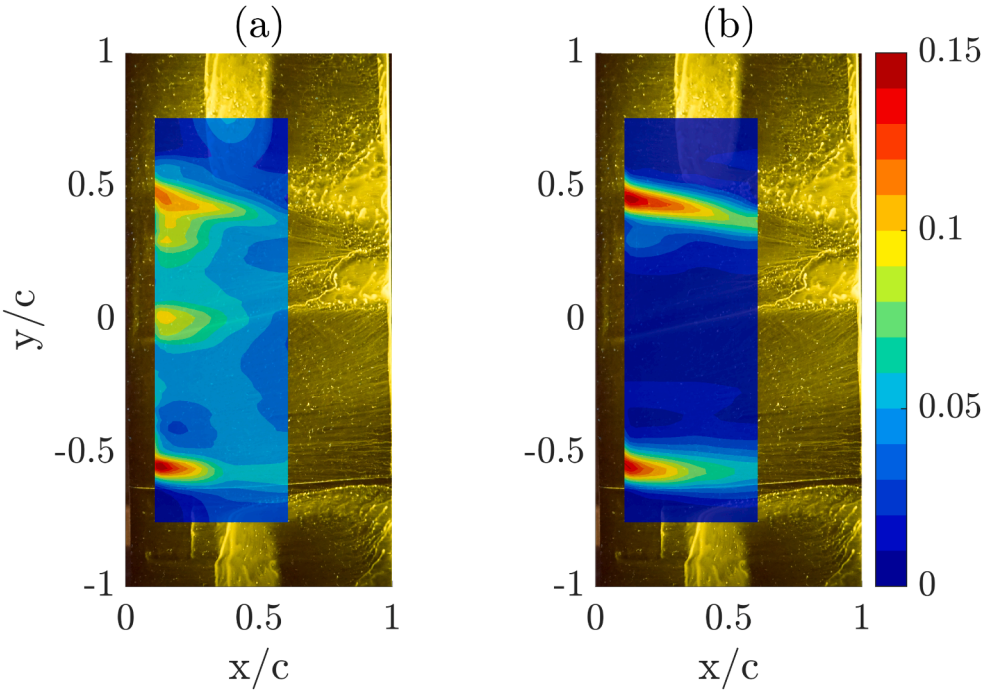

Fig. 15. Overlay of the pressure rms on the oil flow visualization at $\alpha = 6°$, $\beta_{\frac{r}{R}=0.7} = 30°$, $J = 0.8$: (a) $C''_{p,rms}$ and (b) $\tilde{C}_{p,rms}$.

4. Results

4.1. Nacelle-only cases

The nacelle-only cases are useful to identify the location of the laminar to turbulent transition and separation lines without the flow distortion induced by the propeller. They also serve as a baseline for evaluating the propeller's effect later. Fig. 5 shows the oil flow visualization obtained for the nacelle-only cases, for which the SES was removed. For the chosen airfoil at the tested Reynolds number (Re_∞) of $\sim 2.6 \cdot 10^5$, a laminar separation bubble (LSB) is formed, as previously described in [33]. By increasing the angle of attack, the LSB is known to move towards the leading edge on the suction side and become thinner [43], as also observed in visualizations in Fig. 5. Lastly, the wake of the nacelle causes the LSB to disappear locally around the midspan of the wing, probably due to a local increase in the inflow turbulence [44].

The $C'_{p,rms}$ for the nacelle-only case at an angle of attack of 6°, overlaid on the oil flow visualization, is shown in Fig. 6. The overlay is performed manually, as an optical calibration prior to taking the images was not performed. It can be seen how the measurement taken from the microphones resembles the oil flow visualization, as the higher pressure fluctuations are found where the LSB is observed in the oil flow. Indeed, laminar separation bubbles are characterized by higher pressure fluctuations with respect to the attached flow, as discussed in [45]. Looking into the spectral content of the pressure fluctuations in different regions allows to distinguish laminar flow from turbulent or separated flow, as each is characterized by a different shape of the pressure spectrum. Fig. 7 shows the evaluated PSD on the suction side at $y/c = 0.4$ at three

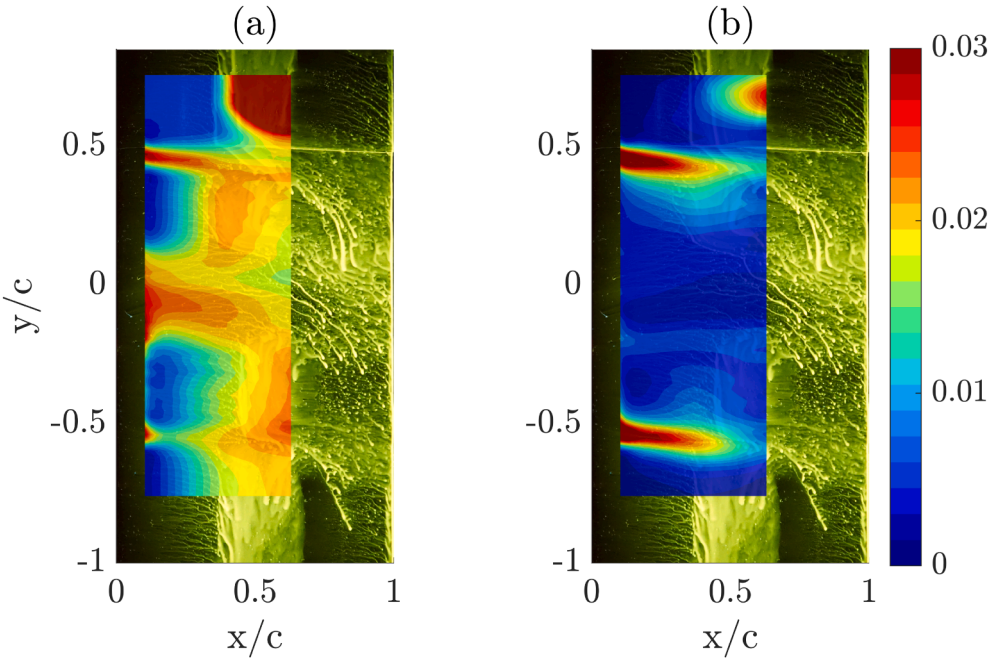

Fig. 16. Overlay of the pressure rms on the oil flow visualization at $\alpha = 0°$, $\beta_{\frac{r}{R}=0.7} = 45°$, $J = 1.8$: (a) $C''_{p,rms}$ and (b) $\tilde{C}_{p,rms}$.

chordwise coordinates. The data is given in terms of the chord-based Strouhal number:

$$St_c = \frac{fc}{U_\infty} \tag{9}$$

where c is the chord of the airfoil and f is the corresponding frequency.

For the selected case, $x/c = 0.37$ falls within the LSB. This is indicated by the presence of a 'hump' on the wall-pressure spectrum for $10 < St_c < 20$, in agreement with the observations reported in [45] and with the oil flow visualization in Fig. 6. The difference between the turbulent and laminar regimes can be appreciated. The PSD corresponding to $x/c = 0.56$ shows stronger fluctuations and energy content at higher frequencies, which decay proportionally to $f^{-5.5}$ as observed in [46], indicating a turbulent flow regime. On the contrary, at $x/c = 0.17$, the pressure spectrum decays faster for increasing frequencies, and the fluctuations have a lower amplitude overall.

4.2. Propeller-wing interaction

The propeller slipstream interacting with the wing strongly modifies the flow structure with respect to the nacelle-only cases. For the $\beta_{\frac{r}{R}=0.7} = 30°$ propeller at $J = 0.8$ (Fig. 8), the LSB disappears from the portion of the wing washed by the propeller slipstream. However, it is still present outside it. A clear distinction is seen between the UBS and DBS: The flow separates earlier in the UBS and stays attached in the DBS even for $\alpha = 12°$, in line with the observations made in [14]. The slipstream deformation is greater at higher angles of attack. For the cases at $\alpha = 9°$ and $\alpha = 12°$, some flow lines from the DBS are directed towards the UBS. A possible explanation for this is that the lower pressure experienced on the UBS generates a pressure gradient that forces flow into that region. The unsteady nature of the problem is not captured by the oil flow visualization, which will be later discussed in detail, based on the data sampled by the SES.

At $\beta_{\frac{r}{R}=0.7} = 45°$ with $J = 1.8$ (Fig. 9) and angle of attack $\alpha = 0°$, the LSB does not fully disappear within the region washed by the propeller slipstream, as for the previous case, but its position changes along the chord. On UBS (induced upwash), the LSB starts closer to the leading edge than outside the slipstream. In contrast, the LSB on the advancing side (induced downwash) is positioned further from the leading edge. A likely reason for this is that the low T_c and high J lead to an angle of attack variation, relative to the nacelle-only case, that is small enough such that it does not induce turbulent transition, and thus, only moves the LSB chordwise position over the wing.

The $\overline{C}_p$ distribution at $\alpha = 6°$ for the propeller having $\beta_{\frac{r}{R}=0.7} = 30°$ operating at $J = 0.8$ is shown in Fig. 10. It is known that the retreating side (Fig. 2b) experiences an increased suction with respect to the baseline case. This occurs because the local angle of attack is increased due to the propeller-induced upwash [6,14]. As a consequence, the region characterized by the lowest pressure is also shifted towards the leading edge. This is also one of the reasons why an earlier separation of the flow is seen in the UBS as discussed for the oil flow visualization images in Fig. 8. Lastly, the low-pressure region close to $y = 0$ is likely to be caused by a combination of the nacelle wake and the blades' root vortices.

The rms of the unsteady pressure coefficient ($C'_{p,rms}$) is reported in Fig. 11. The trace of the propeller tip vortices represents the region of pressure fluctuations with the maximum amplitude on the wing. A region of high-pressure fluctuations is also detected close to $y = 0$, which supports the observation made for the low-pressure region seen in the $\overline{C}_p$ distribution at the same location, stating that the cause might be a combination of the nacelle wake and the propeller root vortex.

The deformation of the slipstream on the suction side and on the pressure side is shown in Figs. 12a and b, respectively. As previously seen in the literature [12,13,47], the slipstream is deflected according to the rotation direction, from the retreating side to the advancing side. The trace of the tip vortices over the suction side at $y > 0$ in Fig. 12a, corresponding to the retreating side, is deflected towards the center of the propeller slipstream, in line with the qualitative results obtained from the oil flow images in Fig. 8. The same occurs on the pressure side ($y < 0$ in Fig. 12b), however, the effect is less pronounced.

For angles of attack equal to 0°, 6°, 9°, and 12°, the rms of the fluctuating pressure coefficient ($C'_{p,rms}$) along the spanwise direction is shown for the suction side in Fig. 13 and for the pressure side in Fig. 14. The

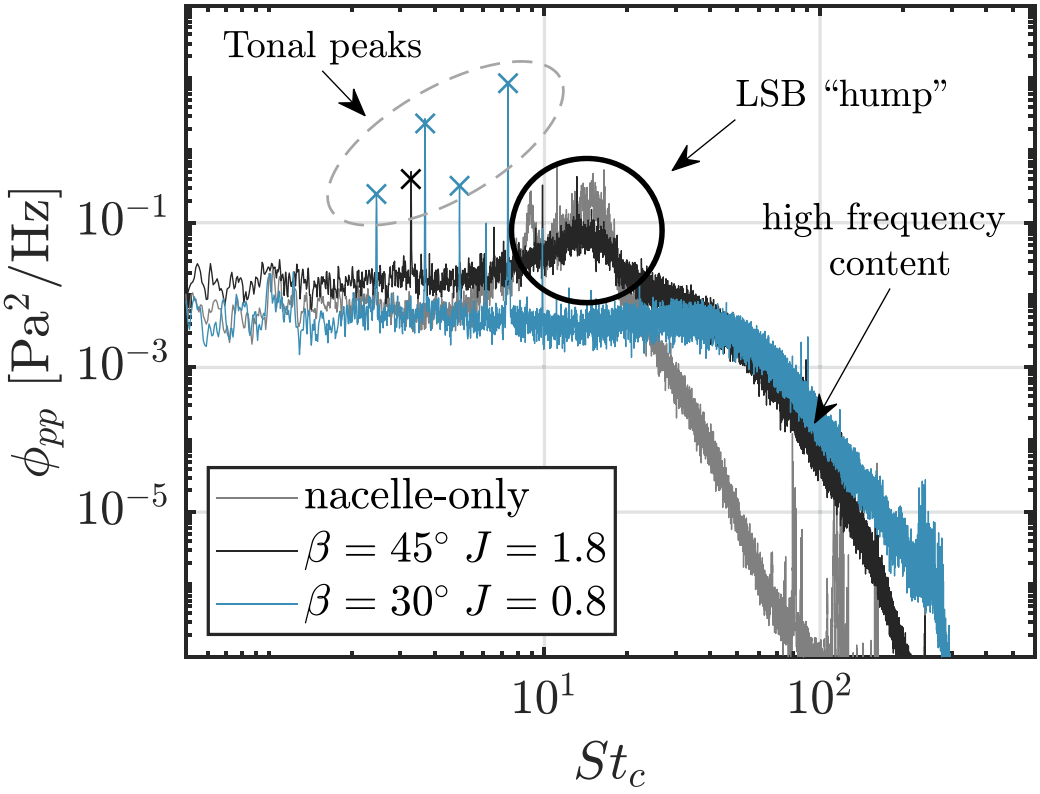

Fig. 17. Wall pressure spectrum evaluated on the suction side at $x/c = 0.55$ and $y/c = 0.58$ ($y/R = 1.14$) at $\alpha = 0°$ for the nacelle-only and propeller-on cases.

dashed lines indicate the spanwise extension of the propeller. To focus on the spanwise distribution, fixed chordwise positions were chosen for the suction side ($x/c = 0.37$) and pressure side ($x/c = 0.32$).

The two peaks at approximately opposite spanwise coordinates close to $y/c = \pm 0.5$, correspond to the location of the tip vortex trace over he wing. On the suction side, a small increase in pressure fluctuations is observed at increasing angles of attack. The peak corresponding to the retreating side ($y > 0$ for the suction side) shifts inboard (to the left), and the effect seems to increase for higher angles of attack, suggesting a more pronounced slipstream deformation. Additionally, the retreating side ($y > 0$) experiences greater pressure fluctuations compared to the advancing side ($y < 0$). For the pressure side (Fig. 14), there is less difference between advancing and retreating sides. Pressure fluctuations increase for increasing angles of attack, in particular for the advancing side ($y > 0$ for the pressure side). Moreover, at a non-zero angle of attack, the pressure fluctuations are more pronounced on the pressure side compared to the suction side. This is likely to be a consequence of the installation, as the propeller does not move together with the wing when changing the angle of attack.

On the suction side, the slipstream is deformed towards $y < 0$, following the rotation direction of the propeller. On the pressure side, the traces of the tip vortices are displaced towards $y > 0$ according to the propeller rotation, as in this case the retreating side corresponds to $y < 0$. Nevertheless, the deformation is less intense, as the traces of the tip vortices are closer to the dashed lines indicating the spanwise extension of the propeller in Figs. 13 and 14.

The unsteady pressure coefficient (C_p') is constituted by the turbulent random fluctuations and the fluctuations originating from the periodic forcing associated with the blade passing frequency (BPF) and its harmonics.

Using the triple decomposition described in Section 2.3, it is possible to separate the pressure field corresponding to the coherent propeller-induced fluctuations ($\tilde{C}_p$), from the stochastic ones (C_p'').

The rms of the purely turbulent fluctuations ($C''_{p,rms}$), shown in Fig. 15a, closely reminds of the oil flow visualization, highlighting how the interaction between the propeller slipstream and the wing cannot be described as the superposition of two distinct effects, as the entire structure of the flow and pressure field are modified [12,48].

The coherent fluctuations ($\tilde{C}_{p,rms}$), shown in Fig. 15b, on the other hand, are mainly limited to the tip vortices' trace. The effect of the blades' wakes is known to be stronger near the wing's leading edge due to vortex impingement, which is not measured in this study. Nevertheless, the propagation of the vortical structures over the wing remains coherent enough so to be isolated by the triple decomposition from the stochastic pressure fluctuations.

The stochastic component captures the LSB outside the slipstream at $y > 0$. Close to $y = 0$, a region of large fluctuations is seen, which is not present in $\tilde{C}_{p,rms}$. A possible interpretation is that the source of these fluctuations might not be related to the propeller but rather linked to the wake of the nacelle, as it is uncorrelated with the propeller rotation frequency. However, the root vortices might be merged with the nacelle and spinner wakes, which could lead to them losing their temporal dependency on the propeller rotation frequency.

The same observations made from the oil flow visualization in Fig. 9, regarding the case at $\alpha = 0°$, with $\beta_{\frac{r}{R}=0.7} = 45°$ at $J = 1.8$, can be extended to the distribution of the rms of the stochastic pressure component ($C''_{p,rms}$). In Fig. 16a the LSB on the retreating side (upwash) is anticipated, while on the advancing side (downwash), it is delayed. As in the previous case, the coherent component, shown in Fig. 16b, is mainly limited to the tip vortices trace.

The effect of the propeller slipstream extends outside of the region defined by the tip vortices' trace. Fig. 17 shows the wall-pressure spectrum (ϕ_{pp}) evaluated on the retreating side at $x/c = 0.55$ and $y/c = 0.58$ ($y/R = 1.14$) for an angle of attack $\alpha = 0°$. For the chosen location, the case having $\beta_{\frac{r}{R}=0.7} = 45°$ at $J = 1.8$ shows the character-

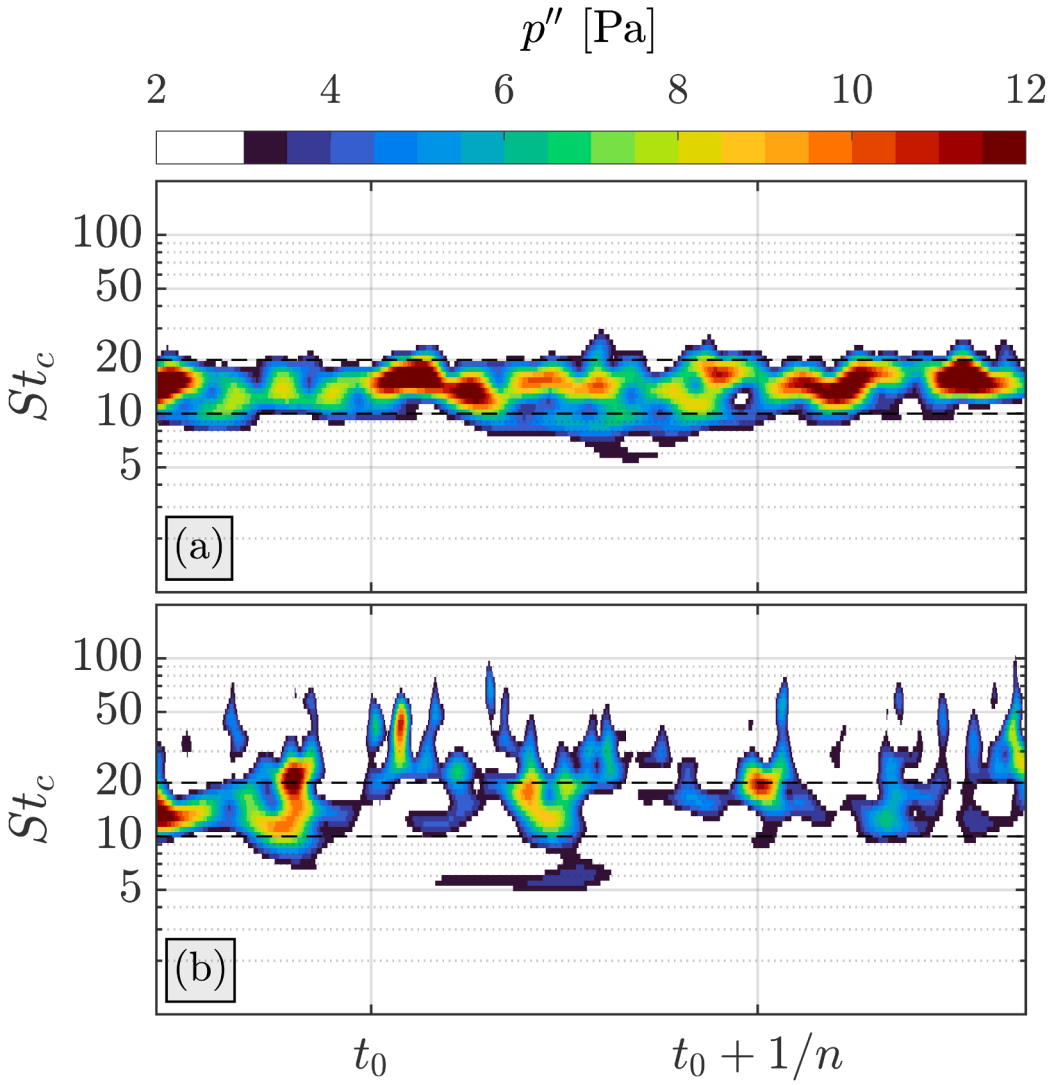

Fig. 18. Wavelet transform of p'' taken at $x/c = 0.55$ and $y/c = 0.58$ with $\alpha = 0°$: (a) nacelle-only case (b) $\beta_{\frac{r}{R}=0.7} = 45°$ at $J = 1.8$; n corresponds to $J = 1.8$.

istic 'hump' associated to an LSB, yet, tonal peaks corresponding to the BPF and its harmonics are also visible. Another interesting finding is the effect on turbulence. The nacelle-only case shows a rapid decay in the energy content for $St_c > 20$. Nevertheless, the propeller-on cases show a high-frequency content associated with turbulent flow. For the case with $\beta_{\frac{r}{R}=0.7} = 30°$ at $J = 0.8$, the LSB is not present, likely due to the higher propeller loading and to the different advance ratio. A lower J means that the distance between consecutive tip vortices is reduced. Moreover, these structures are convected faster, as the higher loading corresponding to a lower J leads to a higher induced velocity inside the propeller slipstream (considering a fixed freestream velocity for the considered cases). This implies that the periodic propeller-shed perturbations interact with the wing boundary layer, triggering its turbulent transition and impeding the formation of an LSB.

For the case with $\beta_{\frac{r}{R}=0.7} = 45°$ at $J = 1.8$, the presence of an LSB and high-frequency content, commonly attributed to turbulence, could be explained in two different ways: 1) An intermittent process [49] might be occurring similar to the work of Miley et al. [50] where the flow is shown to undergo laminar to turbulent transition at each blade passage, leading to the LSB existing only for a fraction of time. 2) The pressure field presents more random fluctuations due to the nearby fluctuating pressure field caused by the propeller slipstream.

Using the wavelet transform, it is possible to describe the behaviour of the pressure signal in both time and frequency, which can be used to evaluate its intermittent nature. Wavelets provide an adaptive resolution that captures the temporal multi-scale nature of turbulence better than the fixed windowing of a spectrogram based on the Fourier transform [51]. This is of particular importance for intermittent signals as shown in [52,53]. Fig. 18a shows the magnitude of the pressure according to the wavelet transform for the same microphone signal taken from the nacelle-only case in Fig. 17, while Fig. 18b shows the same for the case with $\beta_{\frac{r}{R}=0.7} = 45°$ at $J = 1.8$. The time interval shown is given in terms of the rotational speed (n) for the case at $J = 1.8$ for direct comparison.

The nacelle-only case shows that the amplitude of the fluctuations changes in time; however, the fluctuations are concentrated in the frequency interval $10 < St_c < 20$, as expected for a laminar separation bubble [45]. It is worth noting that, in the absence of a coherent forcing, p' and p'' coincide.

For the propeller-on case, in the low loading condition considered here, an intermittent process is observed. During a revolution (indicated from t_0 to $t_0 + \frac{1}{n}$), fluctuations in the $10 < St_c < 20$ range are not always present; in addition, fluctuations at higher frequencies (i.e. $St_c \sim 40$) are observed with a certain periodicity, likely associated with the blade passing frequency. This suggests that the LSB does not always exist, opposite to the case in Fig. 18a.

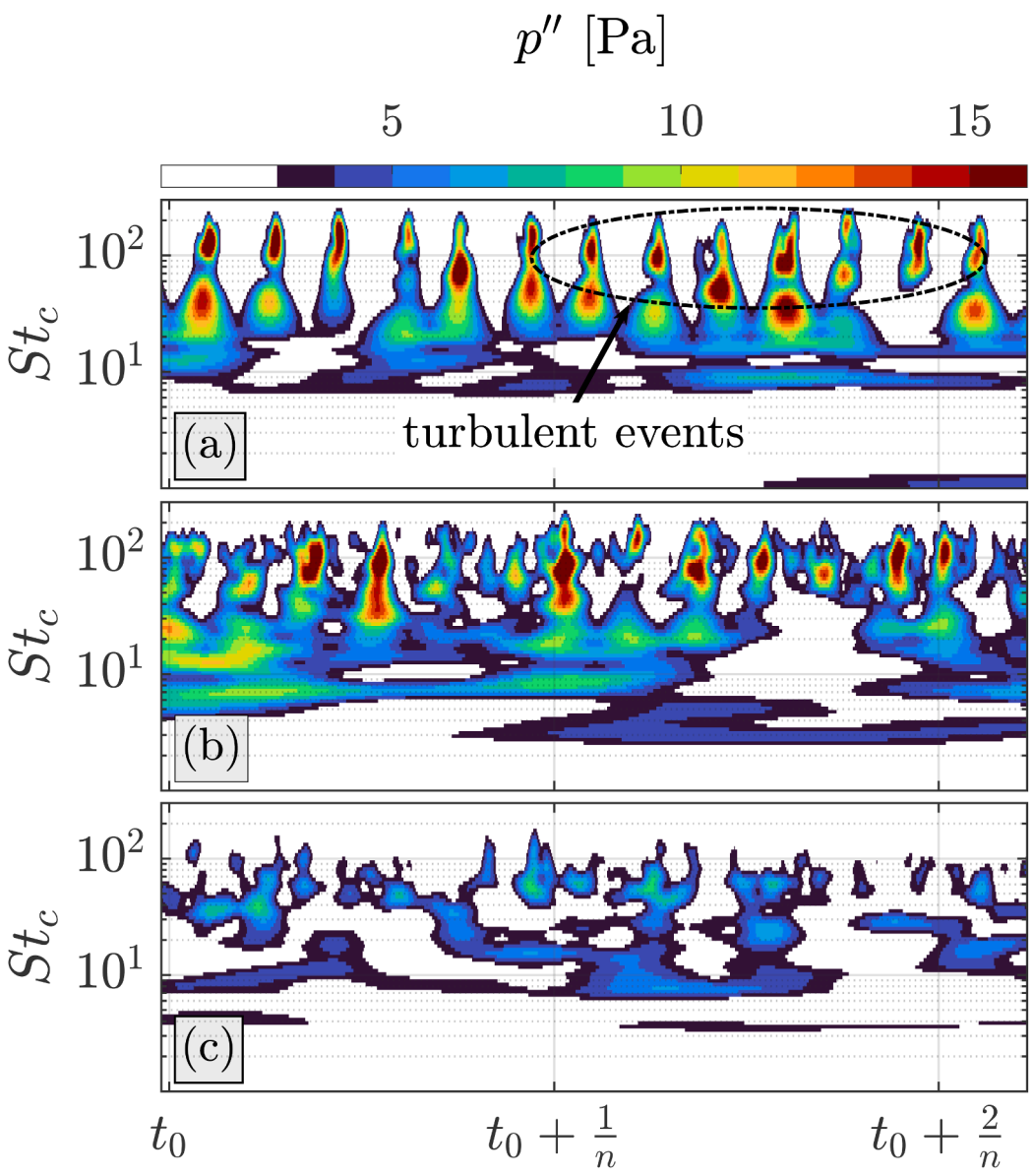

Fig. 19. Wavelet transform of p'' for the case with $\beta_{\frac{r}{R}=0.7} = 30°$ at $J = 0.8$ with $\alpha = 6°$, $(x/c\,, y/c)$ coordinates: (a) $(0.17, 0.46)$, (b) $(0.37, 0.40)$, (c) $(0.55, 0.34)$.

The trace of the vortices over the wing corresponds to the region where the pressure fluctuations are stronger (as in Fig. 11) and are expected to be more coherent. Focusing on the tip vortices traces, the evolution of these structures can be assessed, and it is expected that they become less coherent going downstream [13]. To this end, the case with $\beta_{\frac{r}{R}=0.7} = 30°$ at $J = 0.8$ was chosen, as the propeller blades induce a stronger circulation, leading to a greater pressure fluctuation over the wing. Fig. 19 shows the wavelet transform of the stochastic pressure signal (p'') in three locations following the tip vortex trace on the up-going blade side at $\alpha = 6°$ (for reference, $y > 0$ in Figure 12a). At $x/c = 0.17$, six distinct turbulent events are seen within a revolution, suggesting that each blade passage induces turbulence that dissipates before the next blade passage. Further downstream, at $x/c = 0.37$, the six blade passages are still roughly distinguishable; however, they are less uniform compared to $x/c = 0.17$. At $x/c = 0.55$, it is no longer possible to discern the blade passages, suggesting that the tip vortex structure is less coherent. Moreover, the magnitude of the fluctuations is reduced going downstream. This is likely due to the interaction of the propeller slipstream with the boundary layer developing on the wing. Being the measurements taken farther downstream, a stronger interaction has occurred, thus leading to a more significant distortion of the signal [13].

5. Conclusions

The presented work introduces the SES, a MEMS sensor-embedded sleeve for unsteady pressure measurements, and applies it to the study of propeller-wing interaction, deepening the understanding by assessing the effects on the surface pressure distribution over the wing.

The SES, based on a flexible printed circuit board (PCB), is able to measure time-average and unsteady pressures, as shown by the validation tests presented involving the NACA 63_3018 [33]. The time-averaged pressure coefficient ($\overline{C}_p$) measured from the pressure taps and from the SES showed an average absolute difference of 0.084. The power spectral density (PSD), evaluated from the microphones, corresponding to the pressure fluctuations inside the boundary layer, is compared with Rozenberg's model [34], showing good agreement between the predicted PSD and the measured one.

An application to the study of propeller-wing interaction is shown. A TUD-XPROP-S propeller is installed upstream of the wing model. Two propeller operating conditions are tested, namely advance ratios of 0.8 and 1.8, and nominal blade pitch angles of 30° and 45°, corresponding to thrust coefficients (T_c) of 0.99 and 0.14, respectively, and representing the maximum efficiency for the given pitch setting.

The measured root mean square of the unsteady pressure coefficient ($C'_{p,rms}$) captures the trace of the tip vortices of the propeller and the slipstream deformation. By performing a triple decomposition of the measured pressure signals, the coherent ($\tilde{C}_p$) and the stochastic (C''_p) pressure fluctuations can be separated. The coherent component is mainly limited to the tip vortex trace, while the stochastic component better captures the region washed by the slipstream, highlighting how the interaction between the propeller slipstream and the wing cannot be described as the superposition of two distinct effects, as the entire structure of the flow and pressure field are modified.

Oil flow visualization is used to qualitatively elucidate the flow evolution over the surface. A laminar separation bubble (LSB) is formed in the nacelle-only cases, typical of the low Reynolds number regime on the chosen airfoil. For the propeller-on cases, an LSB was not observed for the high loading case, while it was still detected at the low loading condition. It is concluded that at low propeller loading conditions, the propeller-induced upwash and downwash shift the LSB forward and backward, respectively, without causing transition to turbulent flow near the leading edge of the profile.

An intermittent behaviour was observed along the tip vortices' trace, where, for each blade passage, turbulence is induced. Furthermore, the fluctuations are reduced downstream, and the structures become less coherent in time.

Besides deepening the understanding in propeller-wing interaction related phenomena, this work serves as a presentation and validation of the sensor-embedded sleeve (SES) for unsteady pressure measurements. The SES requires minimal installation considerations, and it can be installed on virtually any surface with a one-directional curvature, without requiring modifications to the target surface, making it a versatile device. This opens the opportunity for applications on surfaces that could not be instrumented otherwise, as flight testing, for instance.

The main limitation of the SES on the presented application was the chordwise spatial resolution. Although it could have been increased by shifting the sleeve in the chordwise direction, similar to the approach used for the spanwise resolution, this would have required further measurements. In addition, these measurements would not be temporally correlated. Nevertheless, this limitation is only due to the sensor's position on the PCB sleeve and to the number of sensors installed on the SES, which could be changed in a redesign of the SES to better suit the intended application. On a final note, the SES is of interest not only for the pressure distribution over an aerodynamic surface but could also be used to unravel the interaction with buildings and/or complex environments.

CRediT authorship contribution statement

P. Comunian: Writing – original draft, Visualization, Methodology, Investigation, Formal analysis, Data curation, Conceptualization, Writing – review & editing; **G. Cafiero:** Writing – original draft, Supervision, Methodology, Investigation, Funding acquisition, Formal analysis; **J. Serpieri:** Writing – review & editing, Supervision, Methodology, Investigation, Formal analysis; **F. Avallone:** Writing – review & editing, Conceptualization; **R. Zamponi:** Writing – review & editing, Methodology, Formal analysis, Conceptualization; **D. Ragni:** Writing – original draft, Supervision, Project administration, Methodology, Funding acquisition, Formal analysis, Conceptualization; **T. Sinnige:** Writing – original draft, Supervision, Project administration, Methodology, Funding acquisition, Formal analysis, Conceptualization.

Data availability

Data will be made available on request.

Declaration of competing interest

The authors declare the following financial interests/personal relationships which may be considered as potential competing interests:

Paolo Comunian reports financial support was provided by MOST Centro Nazionale per la Mobilità Sostenibile. If there are other authors, they declare that they have no known competing financial interests or personal relationships that could have appeared to influence the work reported in this paper.

Acknowledgement

The authors thank Adithya Ramesh and Hans van der Does for the design and construction of the sensor sleeve, Rolf Kalbermatter for the development of the data acquisition software, as well as Prantik Dutta, Srivatsav Swaminathan, Aaron Sequeira, and Buğrahan Öztürk for their help in conducting the experiments.

PC and GC were supported by *MOST - Sustainable Mobility National Research Center* and received funding from the *European Union Next-GenerationEU (PIANO NAZIONALE DI RIPRESA E RESILIENZA (PNRR) - MISSIONE 4 COMPONENTE 2, INVESTIMENTO 1.4 - D.D. 1033 17/06/2022, CN00000023)*. This manuscript reflects only the authors' views and opinions, neither the European Union nor the European Commission can be considered responsible for them.

References

[1] M.A. Rendón, C.D. Sánchez R, J. Gallo M, A.H. Anzai, Aircraft hybrid-electric propulsion: development trends, challenges and opportunities, J. Contr. Autom. Electr. Syst. 32 (5) (2021) 1244–1268.
[2] L.M. Cardone, G. Petrone, S. De Rosa, F. Franco, C.S. Greco, Review of the recent developments about the hybrid propelled aircraft, Aerotec. Missili Spazio 103 (1) (2024) 17–37.
[3] R. De Vries, M. Brown, R. Vos, Preliminary sizing method for hybrid-electric distributed-propulsion aircraft, J. Aircr. 56 (6) (2019) 2172–2188.
[4] L.L.M. Veldhuis, Propeller wing aerodynamic interference, PhD Dissertation, Delft University of Technology (2005).
[5] T. Sinnige, N. van Arnhem, T.C.A. Stokkermans, G. Eitelberg, L.L.M. Veldhuis, Wingtip-mounted propellers: aerodynamic analysis of interaction effects and comparison with conventional layout, J. Aircr. 56 (1) (2019) 295–312.
[6] P. Comunian, J. Serpieri, G. Cafiero, A genetic-algorithm based approach for optimized distributed propulsion, in: AIAA Aviation Forum and Ascend 2024, 2024, p. 3603.
[7] P. Comunian, J. Serpieri, G. Cafiero, A numerical framework for multiparametric optimization of distributed electric propulsion, J. Aircr. (2025) 1–11.
[8] R. Nederlof, J. Goyal, T. Sinnige, D. Ragni, L.L.M. Veldhuis, Fast numerical modeling of propeller–wing aerodynamic interactions, AIAA J. (2025) 63(6), 2025, 2499–2519.
[9] M.D. Patterson, J.M. Derlaga, N.K. Borer, High-lift propeller system configuration selection for NASA's SCEPTOR distributed electric propulsion flight demonstrator, in: 16th AIAA Aviation Technology, Integration, and Operations Conference, 2016, p. 3922.
[10] E. De Paola, R. Camussi, G.L. Stoica, A. Di Marco, G. Capobianchi, Aerodynamic and aeroacoustic experimental investigation of a three propellers DEP configuration, Aerosp. Sci. Technol. 154 (2024) 109508.
[11] D.P. Witkowski, A.K.H. Lee, J.P. Sullivan, Aerodynamic interaction between propellers and wings, J. Aircr. 26 (9) (1989) 829–836.
[12] T. Sinnige, R. De Vries, B.D. Corte, F. Avallone, D. Ragni, G. Eitelberg, L.L.M. Veldhuis, Unsteady pylon loading caused by propeller-slipstream impingement for tip-mounted propellers, J. Aircr. 55 (4) (2018) 1605–1618.
[13] M. Felli, Underlying mechanisms of propeller wake interaction with a wing, J. Fluid Mech. 908 (2021) A10.
[14] M. Okawa, R. Nishimura, T. Ikami, H. Nagai, Unsteady propeller wake interference on wing in tractor configuration at low-Reynolds-number condition, J. Aircr. 62 (1) (2025) 3–12.
[15] N.S. Zawodny, D.D. Boyd, D.M. Nark, Aerodynamic and acoustic interactions associated with inboard propeller-wing configurations, in: AIAA Scitech 2021 Forum, 2021, p. 0714.
[16] Y. Furusawa, K. Kitamura, Unsteady numerical simulation on angle-of-attack effects of tractor-propeller/wing and pusher-propeller/wing interactions, in: AIAA Scitech 2020 Forum, 2020, p. 1030.
[17] R.K. Amiet, Noise due to turbulent flow past a trailing edge, J. Sound Vib. 47 (3) (1976) 387–393.

[18] M.S. Howe, A review of the theory of trailing edge noise, J. Sound Vib. 61 (3) (1978) 437–465.
[19] J.A. Cockburn, J.E. Robertson, Vibration response of spacecraft shrouds toin-flight fluctuating pressures, J. Sound Vib. 33 (4) (1974) 399–425.
[20] J. da Rocha, A. Suleman, F. Lau, Flow-induced noise and vibration in aircraft cylindrical cabins: closed-form analytical model validation, (2011) J. Vib. Acoust., 133(5) 051013.
[21] S. Park, G.C. Lauchle, Wall pressure fluctuation spectra due to boundary-layer transition, J. Sound Vib. 319 (3–5) (2009) 1067–1082.
[22] P. Nikoueeyan, M.D. Hind, J. Strike, M. Perry, B. Wimpenny, L. Mears, P.R. Shea, J. Collins, M.A. Walker, J.T. Pinier, et al., Evaluating the utility of pressure scanners for unsteady pressure measurements in wind tunnel characterization of the space launch system, in: AIAA AVIATION 2022 Forum, 2022, p. 3666.
[23] S. Discetti, A. Ianiro, Experimental Aerodynamics, CRC Press, 2017.
[24] C. Sardu, D. Lasagna, G. Iuso, Noise filtering for wall-pressure fluctuations in measurements around a cylinder with laminar and turbulent flow separation, J. Fluids Eng. 138 (6) (2016) 061101.
[25] M. Roger, Microphone measurements in aeroacoustic installations, Educ. notes, stoen-avt-287, S&T Organ. (2017).
[26] D. Fritsch, V. Vishwanathan, T. Lowe, W.J. Devenport, The effect of grazing flow on pinhole condenser microphones, in: AIAA Scitech 2021 Forum, 2021, p. 0130.
[27] J.W. Gregory, H. Sakaue, T. Liu, J.P. Sullivan, Fast pressure-sensitive paint for flow and acoustic diagnostics, Annu. Rev. Fluid Mech. 46 (1) (2014) 303–330.
[28] N. Maluf, An introduction to microelectromechanical systems engineering, Meas. Sci. Technol. 13 (2) (2002) 229–229.
[29] A. Schwenck, T. Grözinger, T. Günther, A. Schumacher, D. Schuhmacher, K. Werum, A. Zimmermann, Characterization of a PCB based pressure sensor and its joining methods for the metal membrane, Sensors 21 (16) (2021) 5557.
[30] E. Daniel, R. Geisler, F. Philipp, T. Ahlefeldt, A. Goudarzi, S. Carsten, Enhancing aeroacoustic wind tunnel studies through massive channel upscaling with mems microphones, in: 30th AIAA/CEAS Aeroacoustics Conference (2024), 2024, p. 3064.
[31] M.P. Sanders, L.D. De Santana, M. Azarpeyvand, C.H. Venner, Unsteady surface pressure measurements on trailing edge serrations based on digital MEMS microphones, in: 2018 AIAA/CEAS Aeroacoustics Conference, 2018, p. 3290.
[32] C. Raab, K. Rohde-Brandenburger, In-flight testing of MEMS pressure sensors for flight loads determination, in: AIAA Scitech 2020 Forum, 2020, p. 0512.
[33] S. Luesutthiviboon, L.T. Lima Pereira, D. Ragni, F. Avallone, M. Snellen, Aeroacoustic benchmarking of trailing-edge noise from NACA 63 3–018 airfoil with trailing-edge serrations, AIAA J. 61 (1) (2023) 329–354.
[34] Y. Rozenberg, G. Robert, S. Moreau, Wall-pressure spectral model including the adverse pressure gradient effects, AIAA J. 50 (10) (2012) 2168–2179.
[35] J. Dominique, J. Van den Berghe, C. Schram, M.A. Mendez, Artificial neural networks modeling of wall pressure spectra beneath turbulent boundary layers, Phys. Fluids 34 (3) 035119 (2022).
[36] R. de Vries, N. van Arnhem, T. Sinnige, R. Vos, L.L.M. Veldhuis, Aerodynamic interaction between propellers of a distributed-propulsion system in forward flight, Aerosp. Sci. Technol. 118 (2021) 107009. https://doi.org/https://doi.org/10.1016/j.ast.2021.107009
[37] R. de Vries, N. van Arnhem, F. Avallone, D. Ragni, R. Vos, G. Eitelberg, L.L.M. Veldhuis, Experimental investigation of over-the-wing propeller–boundary-layer interaction, AIAA J. 59 (6) (2021) 2169–2182.
[38] M. Drela, XFOIL: an analysis and design system for low Reynolds number airfoils, in: Low Reynolds Number Aerodynamics: Proceedings of the Conference Notre Dame, Indiana, USA, 5–7 June 1989, Springer, 1989, pp. 1–12.
[39] M. Drela, M.B. Giles, Viscous-inviscid analysis of transonic and low Reynolds number airfoils, AIAA J. 25 (10) (1987) 1347–1355.
[40] P. Baj, P.J.K. Bruce, O.R.H. Buxton, The triple decomposition of a fluctuating velocity field in a multiscale flow, Phys. Fluids 27 (7) 075104 (2015).
[41] G. Cafiero, G. Castrillo, C.S. Greco, T. Astarita, On the effects of square-fractal turbulators on the flow field generated by a synthetic jet actuator, Exp. Therm Fluid Sci. 102 (2019) 302–315.
[42] C.S. Greco, G. Cardone, J. Soria, On the behaviour of impinging zero-net-mass-flux jets, J. Fluid Mech. 810 (2017) 25–59.
[43] R. Hain, C.J. Kähler, R. Radespiel, Dynamics of laminar separation bubbles at low-Reynolds-number aerofoils, J. Fluid Mech. 630 (2009) 129–153.
[44] S. Hosseinverdi, H.F. Fasel, Numerical investigation of laminar–turbulent transition in laminar separation bubbles: the effect of free-stream turbulence, J. Fluid Mech. 858 (2019) 714–759.
[45] A. Ducoin, J.A. Astolfi, Wall-pressure fluctuations of laminar separation bubble based on direct numerical simulation and experiments over a hydrofoil at Re = 450,000, Eur. J. Mech. B/Fluids 76 (2019) 132–144.
[46] B.E. McGrath, R.L. Simpson, Some features of surface pressure fluctuations in turbulent boundary layers with zero and favorable pressure gradients, Technical Report, NASA, 1987.
[47] G.K. Ananda, M.S. Selig, R.W. Deters, Experiments of propeller-induced flow effects on a low-Reynolds-number wing, AIAA J. 56 (8) (2018) 3279–3294.
[48] R. Duivenvoorden, N. Suard, T. Sinnige, L.L. Veldhuis, Experimental investigation of aerodynamic interactions of a wing with deployed fowler flap under influence of a propeller slipstream, in: AIAA Aviation 2022 Forum, 2022, p. 3216.
[49] U. Frisch, A.N. Kolmogorov, Turbulence: The Legacy of AN Kolmogorov, Cambridge university press, 1995.
[50] S.J. Miley, R.M. Howard, B.J. Holmes, Wing laminar boundary layer in the presence of a propeller slipstream, J. Aircr. 25 (7) (1988) 606–611.
[51] M. Farge, et al., Wavelet transforms and their applications to turbulence, Annu. Rev. Fluid Mech. 24 (1) (1992) 395–458.
[52] R. Camussi, G. Guj, Orthonormal wavelet decomposition of turbulent flows: intermittency and coherent structures, J. Fluid Mech. 348 (1997) 177–199.
[53] S. Meloni, E. de Paola, E. Grande, D. Ragni, L.G. Stoica, A. Di Marco, R. Camussi, A wavelet-based separation method for tonal and broadband components of low Reynolds-number propeller noise, Meas. Sci. Technol. 34 (4) (2023) 044007.